
ProtoS-ViT: Visual foundation models for sparse self-explainable classifications

Hugues Turbé^{1*}

Mina Bjelogrić¹

Gianmarco Mengaldo²

Christian Lovis¹

¹ Division of medical information sciences, University hospitals of Geneva and Department of radiology and medical informatics, University of Geneva, Switzerland

² Department of Mechanical Engineering, College of Design and Engineering, National University of Singapore, Singapore

Abstract

Prototypical networks aim to build intrinsically explainable models based on the linear summation of concepts. However, important challenges remain in the transparency, compactness, and meaningfulness of the explanations provided by these models. This work demonstrates how frozen pre-trained ViT backbones can be effectively turned into prototypical models for both general and domain-specific tasks, in our case biomedical image classifiers. By leveraging strong spatial features combined with a novel prototypical head, ProtoS-ViT surpasses existing prototypical models showing strong performance in terms of accuracy, compactness, and explainability. Model explainability is evaluated through an extensive set of quantitative and qualitative metrics which serve as a general benchmark for the development of prototypical models. Code is available at <https://github.com/hturbe/protosvit>.

1 Introduction

As deep learning (DL) models are increasingly used for decision making, transparency is becoming a critical issue. Lack of transparency has been repeatedly identified as a key barrier for adoption of DL models in high-risk areas, including the healthcare sector [1]. Transparency encompasses different aspects including AI awareness and model outcome explainability [2]. Outcome explainability aims to understand how a DL model used its input features to produce a given output and has been mainly achieved through post-hoc interpretability methods. These methods typically provide a relevance or saliency map that reveals the importance of each input feature [3] to a certain output. Post-hoc interpretability methods have some attractive properties: they are model agnostic (e.g. SHAP [4]), and they do not affect the performance of the underlying DL model. However, they suffer from some critical drawbacks, namely lack of faithfulness to explaining the model [5, 6, 7], sensitivity to negligible perturbations [8, 9], and high computational cost [10]. This work aims to develop models which are explainable by design, or self-explainable, bypassing the need for post-hoc interpretability, and avoiding altogether the issues associated with them. Before introducing the specific approach adopted, it is useful to define the key properties or pillars that a model should possess to be deemed explainable. The first two have been independently defined both for post-hoc

*Corresponding author: hugues.turbe@unige.ch

interpretability methods [4] and self-explainable models (SEMs) [11]. These are (i) *accuracy*: the explanation accurately depicts the contributions of each input feature to the model’s output, and (ii) *transparency*: the interaction across input features should be understandable by a human. Recently Nauta et al. proposed the Co-12 explanation quality properties for part-prototype image classifiers interpretability [12]. They define (iii) *compactness*: the number of explanations should be reasonably small to allow humans to grasp them easily and rapidly, and (iv) *contrastivity*: explanations should be not overlapping as well as discriminative. This latter property is in line with research on how humans store limited and conceptually distinctive concepts for classification tasks efficiently [13]. Finally, recent works expressed three additional desiderata for interpretability, related to the need to provide semantically coherent concepts [14, 15]. We refer to these three additional properties as (v) *meaningfulness*: the explanations should be semantically understandable to humans, (vi) *completeness* (also referred as additivity in the literature): the explanation should capture all input features playing a role in the model’s predictions, and (vii) *composition*: the full explanations should be shown to the user, to avoid any false impression of explainability.

To achieve these seven pillars of explainability, we developed a novel DL architecture, namely **ProtoS-ViT**, based on visual foundation models, that uses prototypical parts of the input associated with semantic concepts. Semantic concepts are coherent entities that we, as humans, can recognize and associate to a certain object or entity. Take as an example a bird, we can define as semantic concepts the beak, the eyes, and the legs, and associate them to the entity bird, or even, to a specific bird entity (i.e., bird species). These semantic concepts or prototypes are then combined and used to classify images. Given the association of semantic concepts to human knowledge, sparse prototype-based classifiers naturally provide human-understandable explanations, making them self-explainable.

ProtoS-ViT achieves *classification performance* comparable to state-of-the-art (SOTA) DL models on several available benchmarks, while producing the most *compact* set of explanations. In addition, the architecture is *less expensive to train* than most SEM, as it does not require the training of the backbone model, that is instead frozen. In summary, the **contributions of this work** are the following.

1. ProtoS-ViT is the first SEM that leverages the use of frozen foundation models (ViT) as the backbone. Hence, there is no need to train the backbone as compared to most of the SEM literature, making this architecture **computationally efficient** to train. In addition the model’s architecture outperforms prototypical models from the literature in terms of explanation faithfulness by leveraging the strong spatial features of these foundation models.
2. ProtoS-ViT design enables compact explanation, using no more than seven prototype for the benchmark datasets which cover both general and biomedical tasks. The architecture tends to better represent **a small number of discriminative concepts** explaining a high proportion of the predicted class. These feature fulfill the seven explainability requirements introduced above.
3. ProtoS-ViT enables leveraging similarities across classes to provide **explanations that are semantically and visually coherent**, with strong spatial alignment. The latter is evaluated with current and adapted metrics enabling a finer evaluation of the model’s explainability. This set of metrics cover the largest aspect of explainability evaluation and could serve as a general benchmark for the development of prototypical models.

The rest of the paper is organized as follows. In section 2, we describe related and competing work. In section 3, we present the novel architecture, namely ProtoS-ViT. In section 4, we show the results of the experiments conducted on several benchmarks, and how ProtoS-ViT compares against other SOTA DL models. Finally, in section 5, we discuss the results and outline the key conclusions of this work.

2 Related Work

Research on outcome explainability using SEMs that are explainable by design has been very active in the last few years. Many self-explainable classifiers are based on prototypes following the ProtoPNet architecture [16]. The main idea behind this architecture is to extract prototypical parts of images associated with semantic concepts. In particular, the neural-network architecture behind prototype-based classifiers extracts embedded patches that can be matched to learned semantic concepts through a similarity measure. This step allows visualizing the importance of each semantic concepts for each model output.

The early ProtoPNet work [16] had relatively poor classification performance, and coarse spatial resolution for the semantic concepts. To address these issues [17, 11] used the layer-wise relevance propagation (LRP) algorithm to project the extracted concepts over the input space. These allowed increasing prototype resolutions but added the drawbacks associated with post-hoc interpretability methods – namely, lack of faithfulness and high sensitivity to perturbations. Different methods were then developed to further improve the classification performance of the models as well as reduce the number of prototypes used by the model to make a decision [18, 19, 20, 15]. These improvements were mainly achieved by devising new ways to create the prototypes as well as introducing new loss to lower the semantic gap between prototypes and meaningful concepts from images.

All the architectures described above use different variations of CNN backbones including VGG [21], ResNet [22] and DenseNet [23], followed by a linear classifier. Other approaches replaced the final linear classifier with a decision tree. For instance, ProtoTree combined a CNN backbone with a decision tree [24], while the ViT-NeT architecture combines a vision transformer (ViT) backbone with a neural tree decoder [25]. One common flaw of the above models, both with CNN and ViT backbones, is the spatial misalignment of explanations: “Here does not correspond to there” [26]. Indeed, most ProtoNet-like architectures are trained end-to-end, i.e., both the backbone and the prototypical head simultaneously. Given that these models have a receptive field that can reach 100% of the initial image, there is no assurance that the embedding of a patch is directly correlated to the same position in the input image. More evidence of the latter issue has also recently been raised by several authors – see e.g., [27, 28].

Based on the competing literature just outlined, we choose DINOv2 [29] and OpenClip [30] as the backbone for general tasks. Both these models have demonstrated strong performance across a range of computer vision benchmarks. DINOv2 is of particular interest as it has been used for unsupervised segmentation tasks achieving SOTA performance and demonstrating the quality of local information obtained with this model [29, 31]. To further demonstrate the versatility of the proposed approach we also apply our model to three Biomedical tasks using the ViT from BioMedCLIP [32]. In this work, we reframe the explainable classification tasks as the segmentation of useful concepts followed by the evaluation of their importance towards the different classes. This framing lends itself naturally to the use of frozen foundation models with strong spatial features.

Overall the methodology presented next improves: 1) the faithfulness of the concepts propagated into the input space with regards to their impact on the model’s decision; 2) the model’s classification accuracy, 3) the global sparsity – i.e., the global number of prototypes used across the classification tasks, and 4) the local sparsity – i.e., the local number of prototypes to make a prediction for a single image. Besides classification accuracy, we argue that explainability is multi-faceted and require extensive evaluation across all pillars described above. The developed model is therefore extensively evaluated using both quantitative metrics and user studies.

3 Methodology

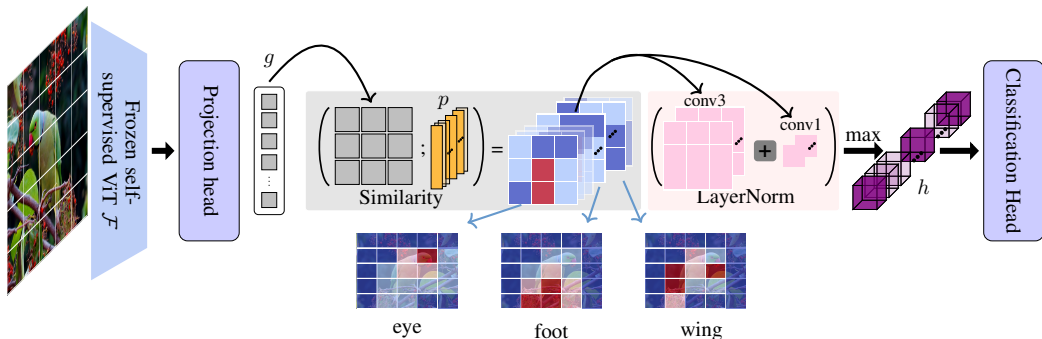


Figure 1: Model architecture. The grey box depicts the similarity head. The pink box indicates the operations forming the prototypical head. Transparency of the elements aims to reflect the model’s sparsity. Bottom: similarity maps interpolated from the similarity head.

Consider a classification task that consists in mapping an image $x \in \mathbb{R}^{H \times W \times C}$ to a labelled target $y \in \mathbb{N}^K$ where H, W, C represent, respectively, the height, width and number of channels of the input image, and K is the number of classes. The input image is fed to a pre-trained feature extractor $\mathcal{F} : x \rightarrow f_i \in \mathbb{R}^{C_e}$ for patch index $i \in [1, \dots, \frac{H}{s} \cdot \frac{W}{s}]$, with s indicating the patch size of the encoder, and C_e the size of the image embedding dimension. In this work, the backbone encoder was DINOv2 and OpenClip for general purpose classification tasks, or BiomedCLIP for medical image classification tasks. The features are then transformed by the *projection head* and compared to learned prototypes. Each prototype is assigned a score by the prototypical head, with this score then being fed to a linear classification head. An overview of the global architecture is depicted in Figure 1 and is described in more detail next along with the process used to produce sparse explanations (notation summarised in Appendix A).

3.1 Prototype matching

This section aims to present the novel architecture developed in this work that matches the features obtained from the pre-trained feature encoder to prototypes with a score that can later be linearly combined to classify the input images. Prototypes are represented as a learnable set of vectors $\mathcal{P} = \{p_j \in \mathbb{R}^D\}$, with $j \in [1, \dots, J]$ where J represents the initial number of learned prototypes and D their dimension.

Following the pre-trained feature extractor, a projection head map consisting of three convolution layers with residual connections maps the features to the corresponding projected features $g_i \in \mathbb{R}^D$. This organization is inspired by [33] for unsupervised segmentation. All convolutions at this stage have a 1×1 kernel size to retain local information. The projected features are then compared to the prototypes by calculating their cosine similarity:

$$S_{i,j} = \cos \langle g_i, p_j \rangle. \quad (1)$$

The prototypes similarity distribution for each patch is then normalised with a softmax function so that the normalised similarity is equal to $\tilde{S}_{i,j} = \sigma_i(S_{i,j}/\tau)$. Including a small temperature τ , in our case $\tau = 0.1$, is key for the network to converge at first and is similar to the similarity measure being often multiplied by a scaling factor to improve convergence in the literature [34, 35].

Once the prototype similarity distribution is known for each patch, the second step aims to determine the importance of the prototype distribution at the image level towards the final class with a novel prototypical head. Most prototypical models only use the maximal value for each prototype across the image as an input to the final classification head [16, 17, 11] such that the prototype score $h_j = \max_i \tilde{S}_{i,j}$. However, this operation prevents the model from learning how the distribution of a prototype presence across the image influences its importance. To tackle this issue, we introduced depthwise convolutions with independent kernels for each prototype. Independent kernels are key for the score to properly reflect the importance of a single prototype presence with no interactions between prototypes. In addition, to model the presence of the prototype at different scales, two convolutions were introduced following insights from the *Inception* architecture [36]; a convolution with a kernel of size 1×1 and another one with size 3×3 . The output of the two convolutions applied to the matrix $\tilde{S}_{i,j}$ is then summed and normalised by a LayerNorm:

$$h_j = \max \left\{ \text{LayerNorm} \left(\text{Conv}_{1 \times 1}(\tilde{S}_j) + \text{Conv}_{3 \times 3}(\tilde{S}_j) \right) \right\}. \quad (2)$$

The max operator is finally applied to the sum and values of h_j below 0.1 are set to 0 when doing inference. The final classification head is then a simple linear classifier with weights W restricted to being positive to improve the explainability of the model. This linear layer takes as input the vector h that indicates the global score of each prototype in the input image. The linear layer converts this score into a class based on the importance of each prototype towards the class of interest. For the rest of the work, we define the importance matrix $\mathbf{I} = (i_{k,j}) \in \mathbb{R}^{K \times J}$ with the importance $i_{k,j}$ of prototype j toward class k as:

$$i_{k,j} = W_{k,j} \times h_j, \quad (3)$$

An important aspect of the proposed architecture is that the concepts are not specific to a single class, allowing the model to learn both similarities and dissimilarities between classes and reducing the overall number of prototypes required to perform a given classification task. This is particularly relevant for tasks where some classes might share many concepts in common, as shown in the experiment section.

3.2 Compact explanations

A key aspect to obtain an useful explainability that satisfies the seven pillars defined in the introduction is that the model should provide a classification using as few concepts as required for a single image (local size of the explanation), as well as using the smallest number of coherent concepts for the entire task (global size). In addition, sparse models have attracted much attention to improve energy efficiency, and, in some cases, model generalization [37].

In our work, to achieve compactness, we use a regularization loss applied on the importance matrix \mathbf{I} , namely the Hoyer-Square (HS) [38]:

$$\mathcal{L}_{HS} = \alpha \frac{|\mathbf{I}|^2}{\|\mathbf{I}\|_2^2} + \gamma \|\mathbf{I}\|_2. \quad (4)$$

In order to minimise the number of concepts used for each prediction, we set $\alpha = \gamma = 0.001$. In addition to these terms, we also adopt the tanh-loss \mathcal{L}_T devised by [15]:

$$\mathcal{L}_T = -\frac{1}{J} \sum_j \log \left(\tanh \left(\sum_i^{I \times B} \tilde{S}_{i,j} \right) + \epsilon \right) \quad (5)$$

where B is the batch size. This last loss is key for the model not to collapse under the pressure of the sparsity loss \mathcal{L}_{HS} at the beginning of the training procedure, enforcing that each prototype is at least present once in each batch. The total loss function is therefore:

$$\mathcal{L} = \mathcal{L}_{CE} + \phi \mathcal{L}_{HS} + \rho \mathcal{L}_T \quad (6)$$

where \mathcal{L}_{CE} is the cross-entropy loss between the model’s prediction and the target, and ϕ the sparsity loss factor.

4 Experiments

To validate the proposed approach, we compare our architecture both with explainable and non-explainable models on a range of datasets. The following section introduces the datasets and implementation details along with qualitative and quantitative evaluation of both classification performance and explainability.

Implementation details. The proposed architecture is implemented in PyTorch [39]. First, all images were resized to a pixel resolution of 224 using random resizing and cropping during training and center cropping at test time. Image augmentation was also performed during training using the AugMix method [40]. The large version of DINOv2, ViT-L/14 with registers [29, 41] as well as OpenCLIP ViT-L/14 [30] were tested as backbone for the general classification tasks. For biomedical tasks, the ViT encoder from BioMedCLIP [32] was used as the backbone. The backbone was frozen and the rest of the architecture trained for 80 epochs, with 10 epochs used for the warm-up. The learning rate (lr) increased linearly during the warm-up to a value of 0.01 with subsequent application of cosine decay. In addition, each model was initialized with 300 prototypes $\mathbf{P} = \{p_j\}_{j=1}^{300}$ with $p_j \in \mathbb{R}^{512}$. Full experimental setups are described in Appendix B.

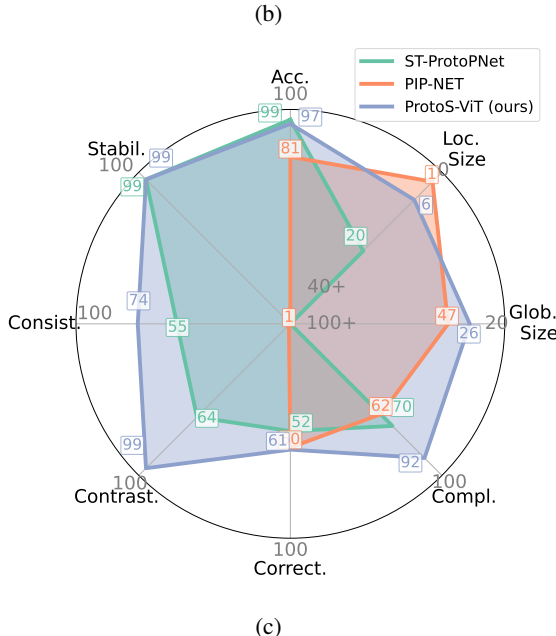
Baselines and datasets. We compare the proposed approach to a non-explainable baseline along SOTA prototypical models. For the non-explainable baseline, we present results for one of the frozen backbone, i.e. DINOv2 ViT-L/14, with a linear classifier reporting results from the initial model publication [29]. In addition, we consider a range of SOTA prototypical models, namely ProtoPNet [16], ProtoTree [24], ProtoPShare [18], ProtoPool [42], PIP-Net [15], ViT-Net [25], ST-ProtoPNet [20], PixPNet [26].

Three common datasets for image classification tasks were used to benchmark the model on general classification tasks: i) CUB-200-2011 [43] (200 bird species), ii) Stanford Cars [44] (196 car models), and iii) Oxford-IIIT Pets (37 cat and dog species) [45]. The proposed architecture was further evaluated on three clinical datasets: i) ISIC 2019 (nine skin lesions type) [46, 47, 48], ii) RSNA pneumonia detection (Presence/absence of a pneumonia on chest radiographs) [49], LC25000 (Lungs): histopathology images with three classes [50]. In addition, we also benchmark our architecture along PIP-Net and ST-ProtoPNet on the recently published FunnyBirds dataset [27] which was specifically developed to evaluate key properties of explainability for DL models. These models were selected

because ST-ProtoPnet consistently achieves the highest accuracy among prototypical models in the literature, while PIP-Net offers the most compact explanations in terms of both local and global size.

General evaluation metrics. We report three quantitative metrics: i) **accuracy**, to evaluate whether the developed architecture is competitive in term of classification performance; ii) **global size**, to measure the total number of prototypes retained by the model to make its predictions across the whole task; and iii) **local size**, to measure the average number of prototypes used to make a prediction on a single image. We restrict the number of local prototypes to the ones used for the predicted class following the definitions in [15]. The metrics are presented for the four general datasets in Panel 1a and for the biomedical tasks in Panel 1b. The accuracy for our model on the CUB dataset is an average over four runs, where the standard deviation was respectively 0.14, 0.11 and 2.9 for the accuracy, local size and global size. Results for the general dataset with the OpenCLIP backbone are presented in Appendix D.

	Method	Acc. Glob.Loc.		Method	Acc. Glob.Loc.			
		↑	Size ↓		Size ↓	Size ↓		
CUB	DINO-L/14	90.5		ISIC	ProtoS-ViT (ours)	77.5	13	4.5
	ProtoPNet	79.2	2000	RSNA	BiomedCLIP	83[†]		
	ProtoTree	82.2	202		ProtoS-ViT (ours)	82.8	9	4
	ProtoPShare	74.7	400	LUNGS	BiomedCLIP	65 [†]		
	ProtoPool	85.5	202		ProtoS-ViT (ours)	100	21	7
	PIP-Net	84.3	495	4				
	ViT-NeT	91.6						
	PixPNet	81.8	10					
	ST-ProtoPNet	86.1	8000					
	ProtoS-ViT (ours)	85.2	39	6				
CARS	DINO-L/14	90.1						
	ProtoPnet	86.1	1960					
	ProtoTree	86.6	195					
	ProtoPShare	86.4	480					
	ProtoPool	88.9	195					
	PIP-Net	88.2	515	4				
	ViT-NeT	93.6						
	ST-ProtoPNet*	92.7	3920					
	ProtoS-ViT (ours)	93.5	54	7				
PETS	DINO-L/14	96.6						
	PIP-NET	92	172	2				
	ProtoS-ViT (ours)	95.2	44	4				
Funny-Birds	ProtoPNET	94.0	500					
	ST-ProtoPNet	99.6	1000	20				
	PIP-NET	81.2	47	1				
	ProtoS-ViT (ours)	96.8	26	6				



Panel 1: (a) Table depicting Accuracy (Acc.), Global Size (Glob. Size), and Local Size (Loc. Size) comparison of different models on general datasets. **Bold** indicates the best score for the given metric (b) Model performance on biomedical dataset with BiomedCLIP as the backbone. (c) Radar plot summarizing model performance both in terms of Accuracy (Acc.) as well as explainability quality with the following metrics Global Size (Glob. Size), and Local Size (Loc. Size), Completeness (Compl.), Correctness (Correct.), and Contrastivity (Contrast.), Consistency (Consist.), and Stability (Stabil.)* Indicates the performance on the cropped version of the dataset. † BiomedCLIP was evaluated on zero shot classification on LUNGS and 100-shot on RSNA. In addition accuracy for both models are extracted from graphs in the corresponding model publication.

We show predictions on two instances from the CUB dataset in Figure 2 with the relative importance of the four most important prototypes for each prediction (more score sheets can be found in

Supplementary materials [51]). The first image in each row shows the location of the four prototypes while the heatmap in the subsequent images represents the similarity map between each patch following the projection head and the corresponding prototype p_j . Given that the ViT output has a reduced spatial dimension (e.g., DINOv2 has a stride of 14 and BiomedCLIP has a stride of 16), we interpolate the similarity map back to the original input resolution. The previous step assumes spatial correlation between the embedding and the input space, the latter being evaluated as part of the carried experiments. Above each prototype, we indicate the corresponding importance, and we retain a consistent color scheme across images to represent identical concepts. Above the first image of each row we show the predicted score as well as the percentage of this score explained by the prototypes shown in the figure.

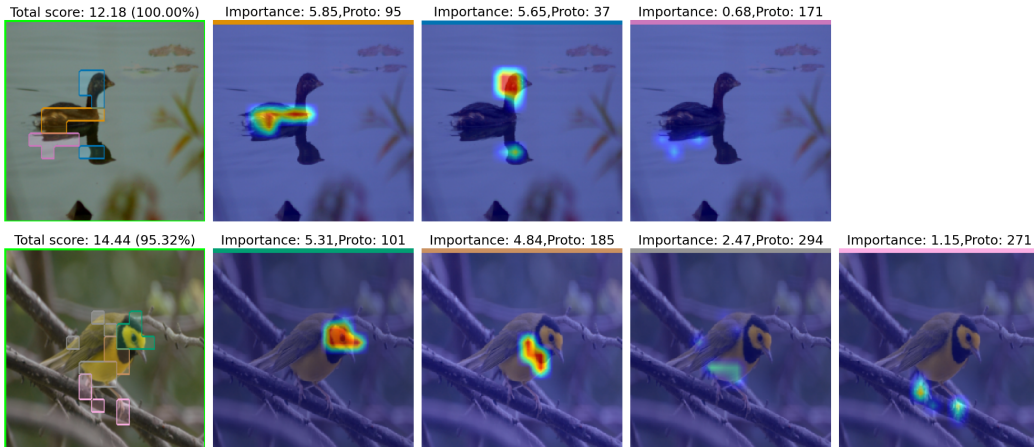


Figure 2: Score sheet for predictions on two random samples of the CUB dataset. Each row shows a prediction on a different sample. The first column indicates the position of the top four prototypes. Each subsequent column shows a prototype along with its importance towards the predicted class. Above the first column, we present the total score for the predicted class as well as how much of this score is explained by the prototypes shown in the figure.

Explainability evaluation metrics The evaluation of explainability is multi-factor with [27] trying to summarize it in three main categories: i) **correctness**, which measures whether the explanations method correctly identifies important and non-important portion of the input with respect to the model; ii) **completeness**, which aims to measure whether a method fully capture the influence of the input on the model’s decision; iii) **contrastivity**, that evaluates whether the explanation method correctly capture parts of the image which are discriminant between classes. These concepts are general to explainable methods (XAI). Following the requirements set out in the introduction, we add that the size of the explanation should be compact, that concepts used by the model should make sense as a coherent group for humans which can serve to categorize a new entity [52], and that the final prediction can be decomposed into the weighted sum of the concepts with their relative importance, similarly to a scoring sheet [15]. In the work by [27], a number of metrics were developed on their synthetic dataset to evaluate requirements i), ii), and iii) described above. The metrics range between zero and one, one being the best. More details on how the framework was adapted to prototypical models as well as details on the different metrics can be found in Appendix F.

The above metrics, while nonspecific to prototypical models, are key to assess the faithfulness of explanations with respect to the model. Interestingly, they encompass a range of metrics previously designed to evaluate prototypical models, see for example [20, 15, 53]. However, these metrics leveraged part-annotations from the CUB dataset leading to some biases. For example, most metrics assumed that pixels activated by the prototypes used for the classification should not lie in the background. The environment of a bird might however be very discriminative in classifying the species it belongs to. To avoid this bias along others described next, the **consistency** and **stability** developed by [53] were adapted to the FunnyBirds dataset. The consistency metric evaluates whether prototypes are mapped to consistent image parts, categories in their article. The stability metric evaluates whether the prototype attribution is stable under perturbations. The latter evaluation is

key as one requirement of prototypical networks is that similarity in the embedding space should reflect similarity in the input space [54]. The latter is not fulfilled if perturbation, invisible to human’s eyes, change the prototypes attribution. The metrics are based on a category activation vector o_p which maps which category, i.e., beak or wing, are found within pixels activated by a given prototype. Huang et al. build this vector by considering a box of a given size around the most activated pixel by prototype j . As highlighted in the literature, this approach might lead to inaccurate evaluation by considering only a very small portion of the input considered by the model [26]. As precise part-annotations are available for the FunnyBirds dataset, we adapt the vector o_p to be equal to one if the similarity map of a prototype is activated within a part-annotation of a given category. More details on the adaptation can be found in Appendix F. This change allows for a finer evaluation of the explanations by considering the full similarity map and not only the top relevance. Panel 1c shows a radar plot of the five explainability evaluation metrics described above along the local and global size of the proposed model. The performance are compared with two SOTA prototypical models, namely PIP-Net and ST-ProtoPNet. The metrics presented in this plot provide an overall evaluation of a model that includes both its performance and the quality of the explanations provided. This quantitative assessment of the quality of the explainability was complemented by two user-studies, one on FunnyBirds and a second one by a clinician on the three biomedical datasets with the results presented in Appendix G.2.

5 Discussion

The development of visual foundation models, often accompanied by text embedding to form CLIP like model, has lead to improved performance across a range of visual tasks. Tasks requiring strong spatial capability, for example semantic segmentation, have vastly benefited from the development of models such as DINOv2. The aim of this work is to develop and evaluate how an architecture could be developed around this type of backbone to create prototypical models that are self-explainable and satisfy the seven interpretability pillars introduced. Based on the three metrics presented in Panel 1a, the developed architecture performs on par or above comparable SOTA prototypical networks in terms of accuracy. ViT-Net achieves the top accuracy on CUB and CARS by combining a non-frozen ViT architecture with a neural tree. Yet, this choice of architecture prevents outcome explainability both in terms of localising important pixels in the input space for the model’s decision as well as case-based reasoning on the extracted prototypes, both issues highlighted in [26].

Accuracy results presented in Panel 1a, show that the designed prototypical network matches or outperforms the non-interpretable baseline across most tasks. The proposed approach therefore allows to build a prototypical model out of a frozen ViT matching the classification performance of the backbone. This observation is also valid for the clinical dataset presented in Panel 1b. Explainability is key for healthcare related tasks and the adoption of DL models in this area [55]. The datasets used in this work cover a wide range of tasks where DL models could improve patient care including classifying skin lesions (ISIC dataset) and chest radiography for the presence of pneumonia (RSNA dataset). The approach presented in this work for biomedical data is even more relevant with more visual foundation model for clinical images being released, for example [56], and being directly usable in the proposed approach.

The evaluation of explainable models and more specifically prototypical models is complex, requiring to go beyond the sole assessment of the classification accuracy. Theoretically prototypical models are of specific interest as they address different drawbacks from post-hoc interpretability methods as discussed in the introduction. An important challenge of this work was to build a comprehensive sets of both quantitative metrics as well as qualitative user studies to allow a general evaluation of the explanations provided by the developed architecture. The quantitative evaluation relies first on the local and global size of the explanation to assess the compactness of the latter. Most prototypical models do not report the local size of the explanations and present score sheet displaying activation maps for few prototypes therefore showing the user only a fraction of the total explanations. This score sheet hence break the completeness and composition requirements set-out by [12]. With a small local size, we are able to show most of the total explanations to the user with simple figures similar to Figure 2. In this figure, the percentage of the total explanation displayed is also indicated to avoid giving the user a false impression of interpretability. In Panel 1c, only PIP-Net has similar local and global size of the explanations, but the ProtoS-ViT outperform this model in terms of accuracy on all benchmarks tasks. A user-study was performed to assess whether the learned prototypes could be

consistently attributed to specific birds parts. This user-study found that prototypes very consistently correspond to a single bird part and full results for this study can be found in Appendix G.2.2.

Overall we observe that the architecture proposed in our work has the lowest global size among the tested architectures and use between six and seven prototypes on average to make a prediction. This indicates that the model strikes a good balance by reusing concepts across classes. The prototypical head was shown in the ablation study, see Appendix E, to greatly reduce the global size of the explanation. This point is important from a user perspective with studies having demonstrated the importance of creating explanations with a limited number of discriminative concepts [13]. The balance is particularly interesting on the CUB dataset and can be visualised by looking at the correlation of the weights from the classification head. These weights assign prototypes to the different classes. Analyses of the correlation across classes of the CUB dataset show that sub-species from a common specie, e.g. woodpecker, have a high correlation indicating that they share a large number of prototypes in common. The details for this evaluation can be found in Appendix G.1. Concept sharing across classes is even more visible on the FunnyBirds dataset, where the distinctive attributes are controlled. The dataset was designed to have a total of 26 concepts split across different beaks, eyes, wings, tails, legs. These elements can be interchanged to create new classes and in their published dataset the authors select 50 classes which are a combination of those concepts. Based on the results presented in Panel 1a, we observe that our model efficiently selects only 26 prototypes, the lowest number of the tested architectures.

The original metrics developed for the FunnyBirds dataset and the proposed adaptation of the consistency and stability metrics allow to evaluate the quality of the explanations both in terms of general explainability as well as with metrics specific to prototypical models. This set of metrics is designed to include the numerous requirements set out in the literature and we envision it as a benchmark for the evaluation of future prototypical models. The radar plot in Panel 1c shows that ProtoS-ViT is the architecture with the top score for overall explainability evaluation as denoted by the overall shaded area as well as all individual metrics. Breaking down the results into the sub-component of the evaluation, it can be observed that ST-ProtoPNET performs relatively well in terms of the faithfulness of its explanation, that is how the similarity maps correctly reflect the importance of the different pixels towards the model classification as evaluated by the contrastivity and correctness metrics. However, ST-ProtoPNET has a lower completeness, meaning that portions of the images outside the explanations actually play a role in the model prediction. In addition, the largest drawback of ST-ProtoPNET is its large local and global size, respectively 20 and 1000 in this case. On the opposite PIP-Net was specifically designed to reduce the local and global size of the explanation but suffer on this benchmark of low performance for the overall quality of the explanation. On this benchmark, training both the backbone and the prototypical head of the model, lead to a collapse of the prototypes with all information regarding the class being encoded in a single patch embedding with no local information. This issue seems particularly pronounced on the FunnyBirds dataset compared to the general benchmark presented in Panel 1a but is a major risk for any prototypical model retraining the backbone without constraining patch embedding to encode local information. This risk was a primary reason for using a frozen backbone, and this design choice was validated by the FunnyBirds benchmark. Our architecture ProtoS-ViT score particularly high for the completeness and contrastivity metrics meaning the explanation highlights all relevant pixels for the model to make a classification and that only relevant pixels are highlighted. The single deletion metric (correctness) is the lowest metric for the developed architecture. Further evaluation showed that the model is robust to part deletion, increasing the contribution of remaining discriminative parts. The initial score might therefore not necessarily decrease under the deletion protocol, which is penalised by this metric. More information and figures related to this observation are presented in Appendix F.

Throughout this work, we developed a novel architecture to provide sparse, visually and semantically meaningful explanations. Through the adoption of a frozen ViT as our backbone as well as a careful design of the overall architecture, the model showed SOTA and beyond classification performance across a range of benchmarks. In addition, our model was superior to other SOTA architectures in terms of sparsity, and meaningfulness of explanations. Indeed, the coherence of the explanations was validated through a range of experiments which were drawn from the literature and adapted to provide a finer evaluation of prototypical networks. Finally, our model is less computationally expensive to train than other architectures as the backbone is frozen. Overall our model demonstrate that visual foundation models can be transformed into explainable classifiers through the training of a

light architecture opening new research areas across a range of different fields e.g., healthcare where explainability will be key.

Acknowledgments and Disclosure of Funding

HT acknowledges financial support from the *fondation Ceres*. GM acknowledges support from MOE Tier 1 grant no. 22-4900-A0001-0: "Discipline-Informed Neural Networks for Interpretable Time-Series Discovery". In addition, all authors thank Julien Ehram, MD for his insightful comments related to the evaluation of the models on biomedical tasks.

References

- [1] Eric J Topol. High-performance medicine: the convergence of human and artificial intelligence. *Nature medicine*, 25(1):44–56, 2019.
- [2] Karen Yeung. Recommendation of the council on artificial intelligence (oecd). *International Legal Materials*, 59(1):27–34, 2020. doi: 10.1017/ilm.2020.5.
- [3] Wojciech Samek, Grégoire Montavon, Sebastian Lapuschkin, Christopher J Anders, and Klaus-Robert Müller. Explaining deep neural networks and beyond: A review of methods and applications. *Proceedings of the IEEE*, 109(3):247–278, 2021.
- [4] Scott M Lundberg and Su-In Lee. A unified approach to interpreting model predictions. *Advances in neural information processing systems*, 30, 2017.
- [5] Julius Adebayo, Justin Gilmer, Michael Muelly, Ian Goodfellow, Moritz Hardt, and Been Kim. Sanity checks for saliency maps. In S. Bengio, H. Wallach, H. Larochelle, K. Grauman, N. Cesa-Bianchi, and R. Garnett, editors, *Advances in Neural Information Processing Systems*, volume 31. Curran Associates, Inc., 2018.
- [6] Dylan Slack, Anna Hilgard, Sameer Singh, and Himabindu Lakkaraju. Reliable post hoc explanations: Modeling uncertainty in explainability. In M. Ranzato, A. Beygelzimer, Y. Dauphin, P.S. Liang, and J. Wortman Vaughan, editors, *Advances in Neural Information Processing Systems*, volume 34, pages 9391–9404. Curran Associates, Inc., 2021.
- [7] Hugues Turbé, Mina Bjelogrić, Christian Lovis, and Gianmarco Mengaldo. Evaluation of post-hoc interpretability methods in time-series classification. *Nature Machine Intelligence*, 5(3):250–260, 2023.
- [8] Amirata Ghorbani, Abubakar Abid, and James Zou. Interpretation of neural networks is fragile. In *Proceedings of the AAAI conference on artificial intelligence*, volume 33, pages 3681–3688, 2019.
- [9] Ann-Kathrin Dombrowski, Maximilian Alber, Christopher Anders, Marcel Ackermann, Klaus-Robert Müller, and Pan Kessel. Explanations can be manipulated and geometry is to blame. *Advances in neural information processing systems*, 32, 2019.
- [10] Guy Van den Broeck, Anton Lykov, Maximilian Schleich, and Dan Suciú. On the tractability of shap explanations. *Journal of Artificial Intelligence Research*, 74:851–886, 2022.
- [11] Srishti Gautam, Ahcene Boubekki, Stine Hansen, Suaiba Salahuddin, Robert Jenssen, Marina Höhne, and Michael Kampffmeyer. Protovae: A trustworthy self-explainable prototypical variational model. *Advances in Neural Information Processing Systems*, 35:17940–17952, 2022.
- [12] Meike Nauta, Jan Trienes, Shreyasi Pathak, Elisa Nguyen, Michelle Peters, Yasmin Schmitt, Jörg Schlötterer, Maurice Van Keulen, and Christin Seifert. From Anecdotal Evidence to Quantitative Evaluation Methods: A Systematic Review on Evaluating Explainable AI. *ACM Comput. Surv.*, 55(13s):1–42, December 2023. ISSN 0360-0300, 1557-7341. doi: 10.1145/3583558. URL <https://dl.acm.org/doi/10.1145/3583558>.

- [13] Talia Konkle, Timothy F. Brady, George A. Alvarez, and Aude Oliva. Conceptual distinctiveness supports detailed visual long-term memory for real-world objects. *Journal of Experimental Psychology: General*, 139(3):558–578, August 2010. ISSN 1939-2222, 0096-3445. doi: 10.1037/a0019165. URL <http://doi.apa.org/getdoi.cfm?doi=10.1037/a0019165>.
- [14] Sunnie S. Y. Kim, Nicole Meister, Vikram V. Ramaswamy, Ruth Fong, and Olga Russakovsky. HIVE: Evaluating the Human Interpretability of Visual Explanations, December 2021. URL <https://arxiv.org/abs/2112.03184v4>.
- [15] Meike Nauta, Jörg Schlötterer, Maurice van Keulen, and Christin Seifert. Pip-net: Patch-based intuitive prototypes for interpretable image classification. In *Proceedings of the IEEE/CVF Conference on Computer Vision and Pattern Recognition*, pages 2744–2753, 2023.
- [16] Chaofan Chen, Oscar Li, Daniel Tao, Alina Barnett, Cynthia Rudin, and Jonathan K Su. This looks like that: deep learning for interpretable image recognition. *Advances in neural information processing systems*, 32, 2019.
- [17] Srishti Gautam, Marina M-C Höhne, Stine Hansen, Robert Jenssen, and Michael Kampffmeyer. This looks more like that: Enhancing self-explaining models by prototypical relevance propagation. *Pattern Recognition*, 136:109172, 2023.
- [18] Dawid Rymarczyk, Łukasz Struski, Jacek Tabor, and Bartosz Zieliński. Protopshare: Prototypical parts sharing for similarity discovery in interpretable image classification. In *Proceedings of the 27th ACM SIGKDD Conference on Knowledge Discovery & Data Mining*, pages 1420–1430, 2021.
- [19] Jon Donnelly, Alina Jade Barnett, and Chaofan Chen. Deformable protopnet: An interpretable image classifier using deformable prototypes. In *Proceedings of the IEEE/CVF Conference on Computer Vision and Pattern Recognition*, pages 10265–10275, 2022.
- [20] Chong Wang, Yuyuan Liu, Yuanhong Chen, Fengbei Liu, Yu Tian, Davis McCarthy, Helen Frazer, and Gustavo Carneiro. Learning support and trivial prototypes for interpretable image classification. In *Proceedings of the IEEE/CVF International Conference on Computer Vision*, pages 2062–2072, 2023.
- [21] K Simonyan and A Zisserman. Very deep convolutional networks for large-scale image recognition. In *3rd International Conference on Learning Representations (ICLR 2015)*. Computational and Biological Learning Society, 2015.
- [22] Kaiming He, Xiangyu Zhang, Shaoqing Ren, and Jian Sun. Deep residual learning for image recognition. In *Proceedings of the IEEE conference on computer vision and pattern recognition*, pages 770–778, 2016.
- [23] Gao Huang, Zhuang Liu, Laurens Van Der Maaten, and Kilian Q Weinberger. Densely connected convolutional networks. In *Proceedings of the IEEE conference on computer vision and pattern recognition*, pages 4700–4708, 2017.
- [24] Meike Nauta, Ron van Bree, and Christin Seifert. Neural prototype trees for interpretable fine-grained image recognition. In *Proceedings of the IEEE/CVF Conference on Computer Vision and Pattern Recognition (CVPR)*, pages 14933–14943, June 2021.
- [25] Sangwon Kim, Jaeyeal Nam, and Byoung Chul Ko. ViT-NeT: Interpretable vision transformers with neural tree decoder. In Kamalika Chaudhuri, Stefanie Jegelka, Le Song, Csaba Szepesvari, Gang Niu, and Sivan Sabato, editors, *Proceedings of the 39th International Conference on Machine Learning*, volume 162 of *Proceedings of Machine Learning Research*, pages 11162–11172. PMLR, 17–23 Jul 2022. URL <https://proceedings.mlr.press/v162/kim22g.html>.
- [26] Zachariah Carmichael, Suhas Lohit, Anoop Cherian, Michael J Jones, and Walter J Scheirer. Pixel-grounded prototypical part networks. In *Proceedings of the IEEE/CVF Winter Conference on Applications of Computer Vision*, pages 4768–4779, 2024.

- [27] Robin Hesse, Simone Schaub-Meyer, and Stefan Roth. Funnybirds: A synthetic vision dataset for a part-based analysis of explainable ai methods. In *Proceedings of the IEEE/CVF International Conference on Computer Vision*, pages 3981–3991, 2023.
- [28] Mikołaj Sacha, Bartosz Jura, Dawid Rymarczyk, Łukasz Struski, Jacek Tabor, and Bartosz Zieliński. Interpretability benchmark for evaluating spatial misalignment of prototypical parts explanations. *arXiv preprint arXiv:2308.08162*, 2023.
- [29] Maxime Oquab, Timothée Darcet, Théo Moutakanni, Huy Vo, Marc Szafraniec, Vasil Khalidov, Pierre Fernandez, Daniel Haziza, Francisco Massa, Alaaeldin El-Nouby, Mahmoud Assran, Nicolas Ballas, Wojciech Galuba, Russell Howes, Po-Yao Huang, Shang-Wen Li, Ishan Misra, Michael Rabbat, Vasu Sharma, Gabriel Synnaeve, Hu Xu, Hervé Jegou, Julien Mairal, Patrick Labatut, Armand Joulin, and Piotr Bojanowski. Dinov2: Learning robust visual features without supervision, 2023.
- [30] Gabriel Ilharco, Mitchell Wortsman, Ross Wightman, Cade Gordon, Nicholas Carlini, Rohan Taori, Achal Dave, Vaishaal Shankar, Hongseok Namkoong, John Miller, Hannaneh Hajishirzi, Ali Farhadi, and Ludwig Schmidt. Openclip, July 2021. URL <https://doi.org/10.5281/zenodo.5143773>. If you use this software, please cite it as below.
- [31] Junho Kim, Byung-Kwan Lee, and Yong Man Ro. Causal unsupervised semantic segmentation. *arXiv preprint arXiv:2310.07379*, 2023.
- [32] Sheng Zhang, Yanbo Xu, Naoto Usuyama, Hanwen Xu, Jaspreet Bagga, Robert Tinn, Sam Preston, Rajesh Rao, Mu Wei, Naveen Valluri, et al. Biomedclip: a multimodal biomedical foundation model pretrained from fifteen million scientific image-text pairs. *arXiv preprint arXiv:2303.00915*, 2023.
- [33] Hyun Seok Seong, WonJun Moon, SuBeen Lee, and Jae-Pil Heo. Leveraging hidden positives for unsupervised semantic segmentation. In *Proceedings of the IEEE/CVF Conference on Computer Vision and Pattern Recognition*, pages 19540–19549, 2023.
- [34] Boris Oreshkin, Pau Rodríguez López, and Alexandre Lacoste. Tadam: Task dependent adaptive metric for improved few-shot learning. *Advances in neural information processing systems*, 31, 2018.
- [35] Cheng Ouyang, Carlo Biffi, Chen Chen, Turkay Kart, Huaqi Qiu, and Daniel Rueckert. Self-supervision with superpixels: Training few-shot medical image segmentation without annotation. In *European Conference on Computer Vision*, pages 762–780, 2020.
- [36] Christian Szegedy, Wei Liu, Yangqing Jia, Pierre Sermanet, Scott Reed, Dragomir Anguelov, Dumitru Erhan, Vincent Vanhoucke, and Andrew Rabinovich. Going deeper with convolutions. In *Proceedings of the IEEE conference on computer vision and pattern recognition*, pages 1–9, 2015.
- [37] Torsten Hoefler, Dan Alistarh, Tal Ben-Nun, Nikoli Dryden, and Alexandra Peste. Sparsity in deep learning: Pruning and growth for efficient inference and training in neural networks. *The Journal of Machine Learning Research*, 22(1):10882–11005, 2021.
- [38] Huanrui Yang, Wei Wen, and Hai Li. Deepfayer: Learning sparser neural network with differentiable scale-invariant sparsity measures. In *International Conference on Learning Representations*, 2019.
- [39] Adam Paszke, Sam Gross, Francisco Massa, Adam Lerer, James Bradbury, Gregory Chanan, Trevor Killeen, Zeming Lin, Natalia Gimelshein, Luca Antiga, et al. Pytorch: An imperative style, high-performance deep learning library. *Advances in neural information processing systems*, 32, 2019.
- [40] Dan Hendrycks, Norman Mu, Ekin Dogus Cubuk, Barret Zoph, Justin Gilmer, and Balaji Lakshminarayanan. Augmix: A simple data processing method to improve robustness and uncertainty. In *International Conference on Learning Representations*, 2019.
- [41] Timothée Darcet, Maxime Oquab, Julien Mairal, and Piotr Bojanowski. Vision transformers need registers. *arXiv preprint arXiv:2309.16588*, 2023.

- [42] Dawid Rymarczyk, Łukasz Struski, Michał Górszczak, Koryna Lewandowska, Jacek Tabor, and Bartosz Zieliński. Interpretable image classification with differentiable prototypes assignment. In Shai Avidan, Gabriel Brostow, Moustapha Cissé, Giovanni Maria Farinella, and Tal Hassner, editors, *Computer Vision – ECCV 2022*, pages 351–368, Cham, 2022. Springer Nature Switzerland.
- [43] Catherine Wah, Steve Branson, Peter Welinder, Pietro Perona, and Serge Belongie. The caltech-ucsd birds-200-2011 dataset. *California Institute of Technology*, 2011.
- [44] Jonathan Krause, Michael Stark, Jia Deng, and Li Fei-Fei. 3d object representations for fine-grained categorization. In *Proceedings of the IEEE international conference on computer vision workshops*, pages 554–561, 2013.
- [45] Omkar M Parkhi, Andrea Vedaldi, Andrew Zisserman, and CV Jawahar. Cats and dogs. In *2012 IEEE conference on computer vision and pattern recognition*, pages 3498–3505. IEEE, 2012.
- [46] Philipp Tschandl, Cliff Rosendahl, and Harald Kittler. The ham10000 dataset, a large collection of multi-source dermatoscopic images of common pigmented skin lesions. *Scientific data*, 5(1): 1–9, 2018.
- [47] Noel CF Codella, David Gutman, M Emre Celebi, Brian Helba, Michael A Marchetti, Stephen W Dusza, Aadi Kalloo, Konstantinos Liopyris, Nabin Mishra, Harald Kittler, et al. Skin lesion analysis toward melanoma detection: A challenge at the 2017 international symposium on biomedical imaging (isbi), hosted by the international skin imaging collaboration (isic). In *2018 IEEE 15th international symposium on biomedical imaging (ISBI 2018)*, pages 168–172. IEEE, 2018.
- [48] Marc Combalia, Noel CF Codella, Veronica Rotemberg, Brian Helba, Veronica Vilaplana, Ofer Reiter, Cristina Carrera, Alicia Barreiro, Allan C Halpern, Susana Puig, et al. Bcn20000: Dermoscopic lesions in the wild. *arXiv preprint arXiv:1908.02288*, 2019.
- [49] George Shih, Carol C Wu, Safwan S Halabi, Marc D Kohli, Luciano M Prevedello, Tessa S Cook, Arjun Sharma, Judith K Amorosa, Veronica Arteaga, Maya Galperin-Aizenberg, et al. Augmenting the national institutes of health chest radiograph dataset with expert annotations of possible pneumonia. *Radiology: Artificial Intelligence*, 1(1):e180041, 2019.
- [50] Andrew A Borkowski, Marilyn M Bui, L Brannon Thomas, Catherine P Wilson, Lauren A DeLand, and Stephen M Mastorides. Lung and colon cancer histopathological image dataset (lc25000). *arXiv preprint arXiv:1912.12142*, 2019.
- [51] Anonymous Athors. Protos-vit dataset, 2024. URL <https://doi.org/10.5281/zenodo.11246712>.
- [52] Lance J. Rips, Edward E. Smith, and Douglas L. Medin. Concepts and Categories: Memory, Meaning, and Metaphysics. In *The Oxford Handbook of Thinking and Reasoning*. Oxford University Press, 03 2012. ISBN 9780199734689. doi: 10.1093/oxfordhb/9780199734689.013.0011. URL <https://doi.org/10.1093/oxfordhb/9780199734689.013.0011>.
- [53] Qihan Huang, Mengqi Xue, Wenqi Huang, Haofei Zhang, Jie Song, Yongcheng Jing, and Mingli Song. Evaluation and improvement of interpretability for self-explainable part-prototype networks. In *Proceedings of the IEEE/CVF International Conference on Computer Vision*, pages 2011–2020, 2023.
- [54] Adrian Hoffmann, Claudio Fanconi, Rahul Rade, and Jonas Kohler. This looks like that... does it? shortcomings of latent space prototype interpretability in deep networks, 2021.
- [55] Julia Amann, Alessandro Blasimme, Effy Vayena, Dietmar Frey, Vince I Madai, and Precise4Q Consortium. Explainability for artificial intelligence in healthcare: a multidisciplinary perspective. *BMC medical informatics and decision making*, 20:1–9, 2020.
- [56] Jun Ma, Yuting He, Feifei Li, Lin Han, Chenyu You, and Bo Wang. Segment anything in medical images. *Nature Communications*, 15(1):654, 2024.

Appendix

A Nomenclature

Table 1: Notations and symbols used in this paper.

	Symbol	Definition
Variables	$x \in \mathbb{R}^{H \times W \times C}$	Sample (image)
	$y \in \mathbb{N}^K$	Labeled target
	K	Number of classes
	H	Sample height
	W	Sample width
	C	Sample number of channels (3 for RGB images)
	s	Patch size of encoder
	$i \in [1, \dots, \frac{H}{s} \cdot \frac{W}{s}]$	patch index
	C_e	Patch embedding dimension
	J	Initial number of prototypes
	$\mathcal{P} = \{p_j \in \mathbb{R}^D\}$	Learnable set of prototypes
	p_j	Prototypes j
	$j \in [1, \dots, J]$	Prototype index
	D	Prototype dimension
	g_i	Projected sample feature i
	$\mathbf{I} = (i_{k,j}) \in \mathbb{R}^{K \times J}$	Importance matrix
	h_j	Prototype score
Operators	$\mathcal{F} : x \rightarrow f_i \in \mathbb{R}^{C_e}$	Encoder operator
	$S_{i,j}$	Cosine similarity between projected sample g_i and prototype p_j
	$\hat{S}_{i,j}$	Normalised cosine similarity

B Experimental Setup

All models were trained on an internal cluster with each model trained on a single NVIDIA GeForce RTX 3090, 12 cores and 64 GB of memory. All models are trained for 80 epochs with an AdamW optimiser and a base learning rate equal to 0.01. The learning is progressively increased for 15 warm-up epochs and then progressively following a cosine-decay schedule. ϕ and ρ were both set equal to 1. With this configuration, individual model were train in between one and three hours.

B.1 Setup for baseline models

ST-ProtoPNet and PIP-Net were trained on the FunnyBirds in order to act as a baseline across the set of metrics presented in this work. Both models were trained following the baseline parameters found in the corresponding article that introduces the respective models. Parameters for ST-ProtoPNet are found in Table 2 and parameters for PIP-Net are listed in Table 3.

Table 2: Hyperparameters for ST-ProtoPNet

Parameter	Value
Backbone model	Densenet 161
Image size	224×224
Batch size	80
Prototype shape	(1000, 64, 1, 1)
Prototype activation function	log
LR joint optimizer	{ features: 1e-4, add on layers: 3e-3, prototype vectors: 3e-3 }
LR joint step size	10
Warm LR	{ add on layers: 3e-3, prototype vector: 3e-3 }
LR last layer	1e-4
Epochs train	20
Warmup epochs	10
Push start	100
Push epochs	[100,110,120]

Table 3: Hyperparameters for PIP-Net

Parameter	Value
Backbone Model	Convnext Tiny 26
Batch Size	16
Batch Size Pretrain	16
Epochs	20
Optimizer	Adam
Learning Rate	0.05
Learning Rate Block	0.0005
Learning Rate Network	0.0005
Weight Decay	0.0
Number of Features	0
Image Size	224
Freeze Epochs	5
Epochs Pretrain	5

C Dataset description

The datasets used in the study are either general purpose datasets (CUB-200-2011, referred as CUB, Stanford Cars, referred as CARS, and Oxford-IIIT Pets referred as PETS), medical datasets (ISIC 2019, RSNA, and LC25000), and one synthetic dataset designed for evaluating part-prototypical models (FunnyBirds). The seven datasets details (including the licence type) are described below:

CUB-200-2011 [43]: The Caltech-UCSD Birds-200-2011 dataset is a dataset containing 11,788 images across 200 bird species. Each species is represented by roughly 60 images, and the dataset includes detailed annotations such as species, bounding boxes, and part locations. The CUB-200-2011 dataset is publicly available and can be used under the Creative Commons Attribution (CC-BY) license.

Stanford Cars [44]: The Stanford Cars dataset contains 16,185 images of 196 classes of cars, with each class typically corresponding to a make, model, and year of a specific car. The dataset includes annotations for the car model, bounding boxes, and viewpoints. The Stanford Cars dataset licence is unknown.

Oxford-IIIT Pets [45]: The Oxford-IIIT Pet dataset consists of 7,349 images of 37 different breeds of cats and dogs. Each image includes a class label, species, and detailed pixel-level segmentation

annotations. The dataset is available under the Creative Commons Attribution-NonCommercial-ShareAlike (CC BY-NC-SA 4.0) license.

ISIC 2019 [46, 47, 48]: The ISIC 2019 dataset contains 25,331 dermoscopic images representing nine different types of skin lesions, with associated ground truth diagnoses. The dataset is part of the International Skin Imaging Collaboration (ISIC) and is available for research purposes under the CC BY-NC 4.0 license.

RSNA Pneumonia Detection [49]: The RSNA Pneumonia Detection Challenge dataset includes 30,000 annotated chest X-ray images, with labels indicating the presence or absence of pneumonia. This dataset was created for the RSNA 2018 Machine Learning Challenge and is freely available for non-commercial use under the terms provided by the RSNA, typically aligning with the CC BY-NC-SA 4.0 license.

LC25000 (Lungs) [50]: The LC25000 dataset includes 25,000 histopathology images of lung tissue, categorized into three classes: lung adenocarcinoma, lung squamous cell carcinoma, and benign lung tissue. The dataset is openly available for research and educational purposes under a Creative Commons Attribution (CC BY 4.0) license.

FunnyBirds [27]: The FunnyBirds dataset consist of 50 500 images (50k train, 500 test) of synthetic 50 bird species. The authors manually designed 5 bird parts: eyes (3 types), beak (4 types), wings (6 types), legs (4 types) and tail (9 types) to construct the 50 classes. The dataset is openly available under the Apache-2.0 licence.

D Results with OpenCLIP backbone

Model performance on the general dataset with OpenCLIP-L backbone are presented in 4.

Table 4: Accuracy (Acc.), Global (Glob.) Size, and Local (Loc.) Size comparison of different models on general datasets with OpenCLIP-Large backbone

	Acc. ↑	Glob. Size ↓	Loc. Size ↓
CUB	79.1	27	5
Cars	93.8	50	6
Pets	93.8	37	4

E Ablation studies

Ablation studies were carried to demonstrate the effectiveness of the prototypical head and sparsity loss. For the experiment without the prototypical head, the latter was replaced with a simple max operation over the similarity matrix \tilde{S} . The experiment without the sparsity loss, was conducted by replacing the loss in equation 4 with an L1 norm on the weight matrix of the classification head. The results of these two experiments are presented in Table 5.

Table 5: Results from the ablation studies, presenting the baseline model compared to the architecture w/o the prototypical head and w/o the sparsity loss. **Bold** indicates the best score for the given metric.

	CUB			Cars			PETS		
	Acc. ↑	Glob. Size ↓	Loc. Size ↓	Acc. ↑	Glob. Size ↓	Loc. Size ↓	Acc. ↑	Glob. Size ↓	Loc. Size ↓
Baseline	85.2	39	6	93.5	54	7	95.2	44	4
w/o prototypical head	85.4	142	20	93.5	148	19	95.9	164	15
w/o sparsity loss	84.6	44	7	92.8	50	7	95.2	44	4

F FunnyBirds methodology and results

The FunnyBirds framework devised by Hesse et al [27] relies on a part importance function $PI(\cdot)$ that needs to be adapted to the chosen explanation method. We adapt the $PI(\cdot)$ to reflect prototypical approaches. For each prototype p_j , we normalise the corresponding similarity map such that it sums to one and then multiply it by the corresponding importance $i_{j,k}$. All metrics computed on the FunnyBirds dataset to evaluate the quality of the explanation are presented for the proposed architecture, as well as for PIP-Net and ST-ProtoPNet in Table 6.

Table 6: FunnyBirds evaluation metrics.

Metric	Abbreviations	Value		
		ST-ProtoPNet	PIP-NET	ProtoS-ViT (ours)
Controlled synthetic data check	CSDC	0.78	0.45	0.94
Preservation check	PC	0.69	0.20	0.97
Deletion check	DC	0.67	0.29	0.92
Distractability	D	0.69	0.92	0.90
Background independence	BI	1	1	1
Single deletion	SD	0.52	0.60	0.61
Target sensitivity	TS	0.64	0.01	0.99
Mean explainability score	mX	0.62	0.41	0.84

The lowest metric for our approach is the single deletion (SD) metric. This metric evaluates whether the relevance attributed to each category: beak, eye, foot, tail and wing is correlated to their influence on the model’s predictions. Figure 3 and Figure 4 help illustrate how the model might be affected as different parts of the birds are removed. First, we observe that as the different parts are individually deleted, the corresponding prototype disappears reinforcing the strong spatial ability of the model. With this experiment, we can see that the local information encoded in the patch embeddings is directly related to the parts highlighted by the similarity. Regarding the single deletion metric, we observe that as a prototype is deleted, this prototype effectively disappears, but the importance of the other remaining prototypes increases. With this increase, the drop in score observed in the predictions with deleted parts cannot be directly related to the importance of the parts and the metric penalizes the model for this increase. However, this increase in the score of the prototypes might also help the model to be more robust as in most cases it is able to make a correct prediction and exploit the redundancy of the parts found in this specific dataset to make a correct prediction.

The metrics from [27] have been calculated for ST-ProtoPNet, PIP-NET and ProtoS-ViT along with the adaptation of Consistency and Stability. They are presented in Table 7 in percentage rather than between zero and one to match the figure in Panel 1c. Contrastivity and Stability could not be calculated for PIP-NET as the explanation was a single patch not overlapping with any bird part, preventing us from running the analysis.

Table 7: Explainability metrics evaluated on the FunnyBirds dataset. Top three metrics come from [27], while the last two are adapted from [53].

Metric	Value		
	ST-ProtoPNet	PIP-NET	ProtoS-ViT (ours)
Completeness	70	62	92
Correctness	52	60	61
Contrastivity	64	1	99
Consistency	55	NA	74
Stability	99	NA	99

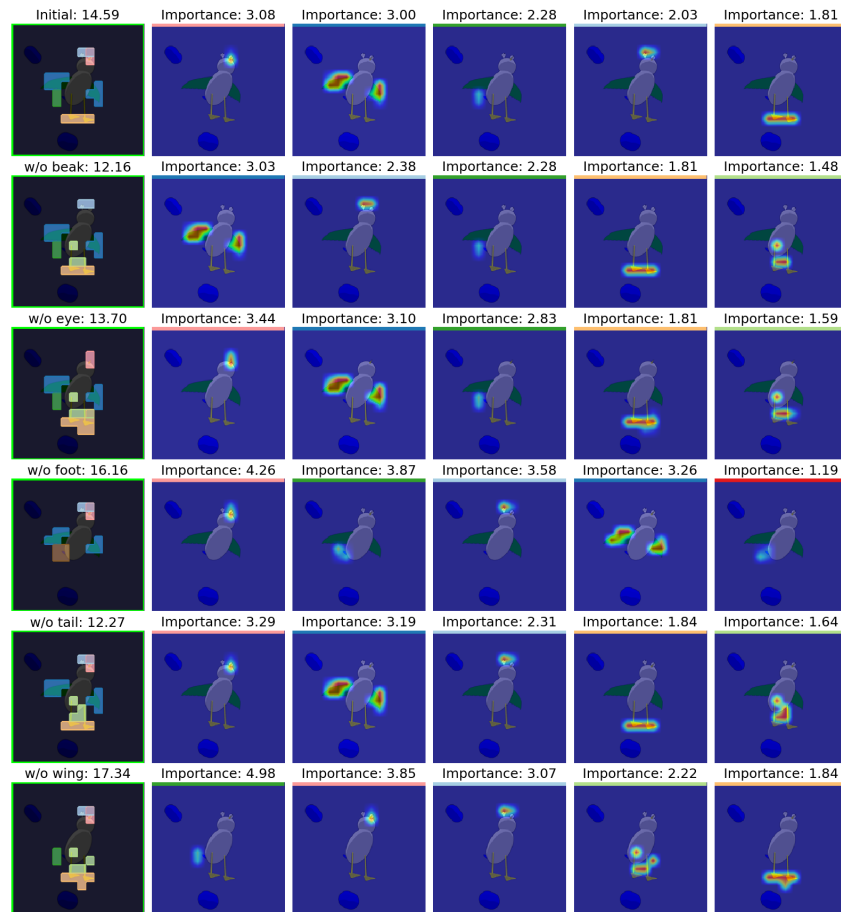


Figure 3: Part deletion analysis on a sample from the FunnyBirds dataset. The first row represent the initial prediction on the non-corrupted sample. Following rows show the model’s predictions along the most important prototypes as different part of the bird are removed. This figure allows to compare the importance attribution of each part with the change in score as this part is removed.

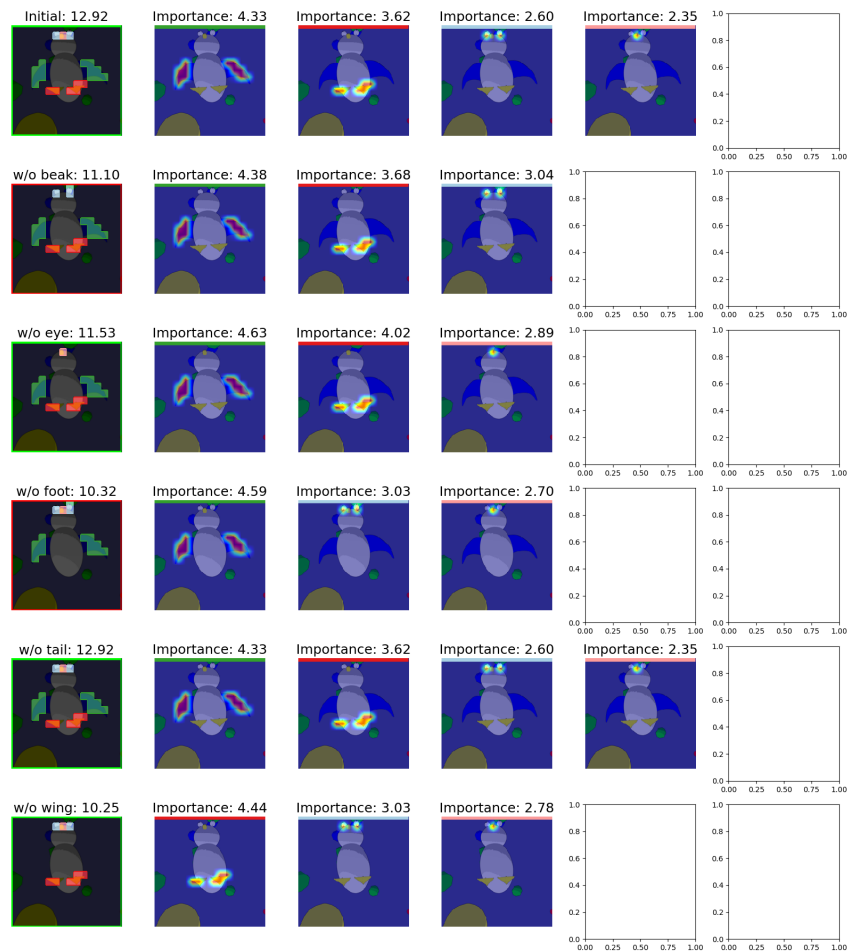


Figure 4: Part deletion analysis on a sample from the FunnyBirds dataset. The first row represent the initial prediction on the non-corrupted sample. Following rows show the model’s predictions along the most important prototypes as different part of the bird are removed. This figure allows to compare the importance attribution of each part with the change in score as this part is removed.

G Evaluation of prototypes quality and semantical consistency

G.1 Classification head correlation

To qualitatively evaluate how the prototypes are reused across classes, we also looked at the correlation of the weights from the classification head. These weights assign prototype to the different classes. Analyses of the correlation across classes of the CUB dataset show that subspecies from a common species have a high correlation across their corresponding vector in the classification weights as measured using the pearson correlation coefficient. Figure 5 shows strong correlation across sparrow subspecies while Figure 6 shows the same level of correlation across both woodpecker and wren. Overall, this analysis shows that prototypes are shared across subspecies effectively sharing prototypes across similar classes.

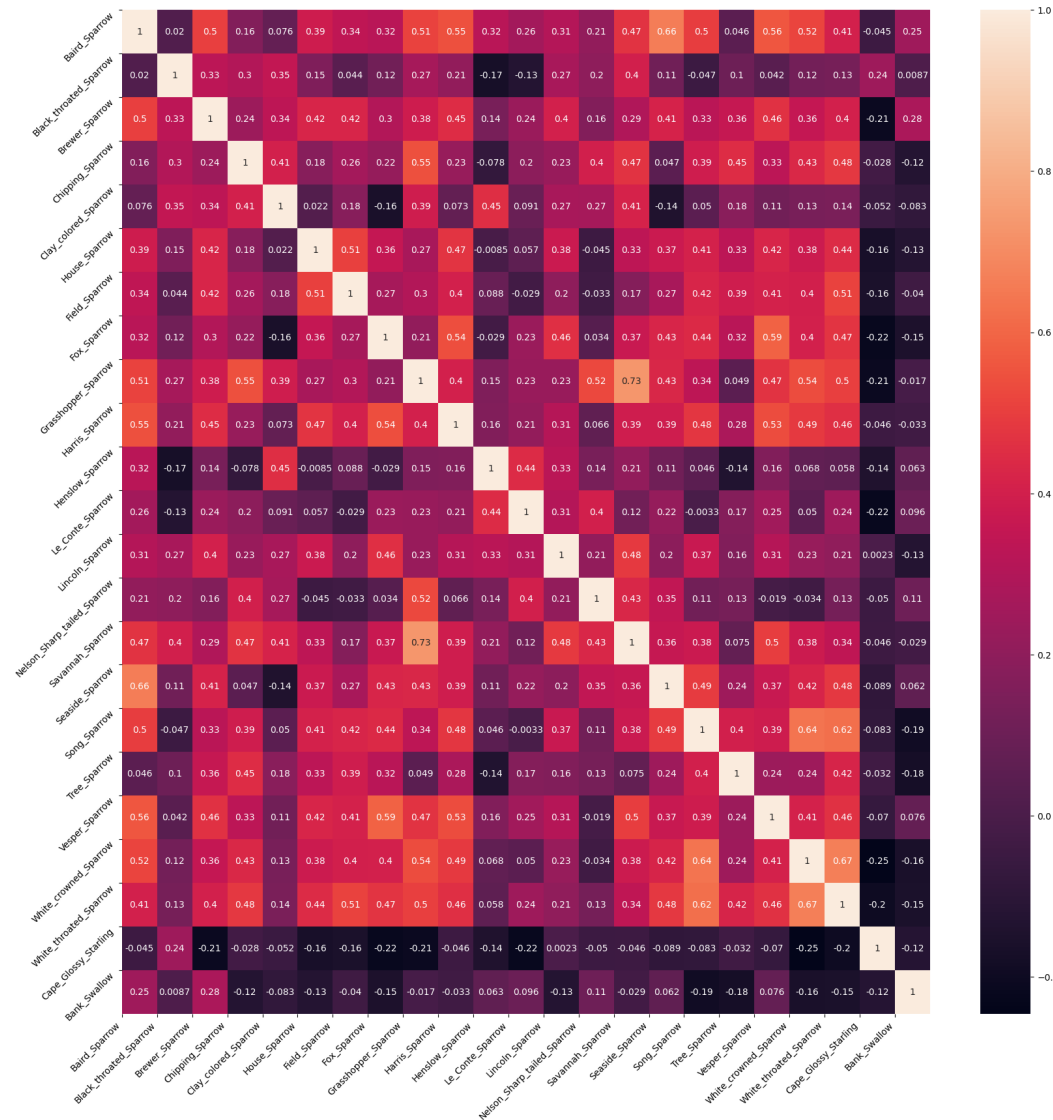


Figure 5: Classification head correlation matrix for classes 112 to 135 of the CUB dataset

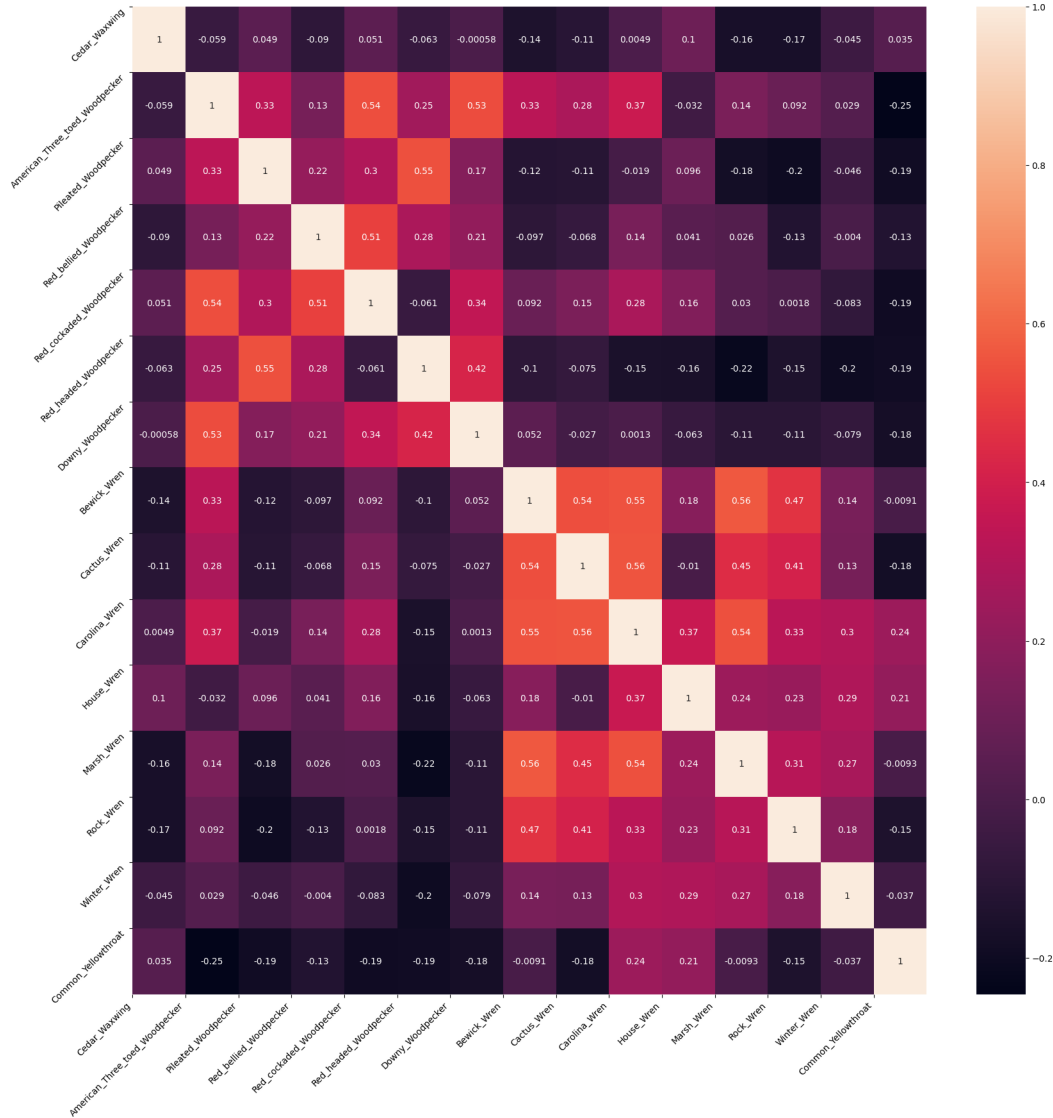


Figure 6: Classification head correlation matrix for classes 112 to 135 of the CUB dataset

G.2 User Study

In addition to the five quantitative metrics used to assess the quality of the explanations provided by the designed architecture, two additional user-studies were carried to better understand the consistency of the prototypes with respect to concepts human would associate together as well as their relevance towards the classifications tasks. The user-studies both rely on a random selection for each prototype of 100 samples where this prototype is playing a role toward the model’s prediction. The first study consisted in a discussion with a clinician who informally described whether the prototypes correspond to the way he would approach the different tasks. As building a fair user-study is difficult on real datasets, the second user-study was carried on the Funny-Birds dataset. Indeed this dataset was designed so that the discriminative portion of each image is well defined by meta-features: the eyes, beak, wings, legs and tail. The samples used for the two user-studies can be found in Supplementary Materials [51].

G.2.1 Clinical datasets

RSNA pneumonia detection dataset: In order to diagnose a pneumonia on chest radiography, clinicians would focus on identifying regions indication opacification of airspace or consolidation of lung parenchyma, specific white regions within lungs. Interestingly, the clinicians saw that prototypes associated with the presence of a pneumonia all lied within the lungs and seemed to possibly identify white regions associated with the opacification/consolidation. However the prototypes associated with the absence of pneumonia all lied outside the lungs and seemed to have no obvious clinical meanings. An explanation for these prototypes, is that the model correctly learned to identify signs of pneumonia and then created some irrelevant prototype so that the score for the absence of a pneumonia increases, similarly to how a bias in the classification head would act. Example of prototypes associate with the absence and presence of pneumonia are presented respectively in Figure 7a and Figure 7b.

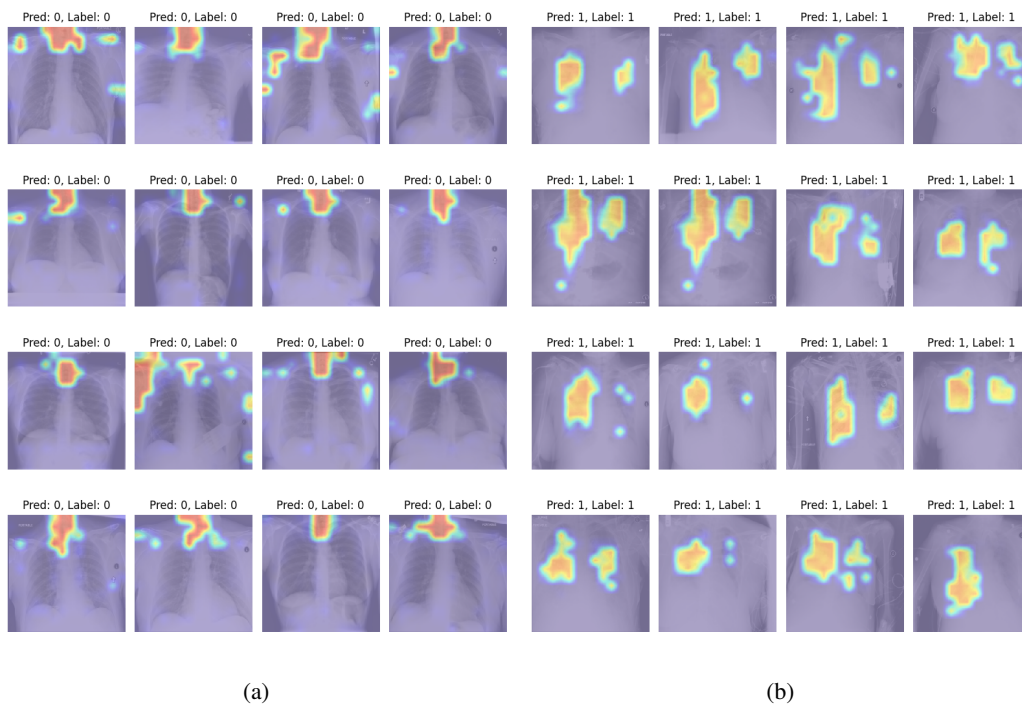


Figure 7: Random sample with activation for a prototype associated with the absence (a) and presence (b) of a pneumonia

ISIC 2019 The classification of skin lesions was reported by the clinicians to be a combinations of different factors, including the symmetry of the lesion, the evenness of the border and the color variation within the skin lesion. The prototype were deemed to correctly reflect a number of these criteria with some prototypes focusing solely on the border, while others seemed to be strongly activated by change in colors of the lesion.

LC25000 Lungs The prototypes for this histopathological dataset were the most difficult to interpret. Diagnostic for this type of image is usually very specific to the area where the tissue is extracted defining the type of cells as well as their frequency within a reference sample. However the clinician found one prototype to look specifically at the nuclei present within a sample possibly indicating that the model assesses the number or size of the nuclei which is a correct indication of malign sample.

G.2.2 Funny Birds

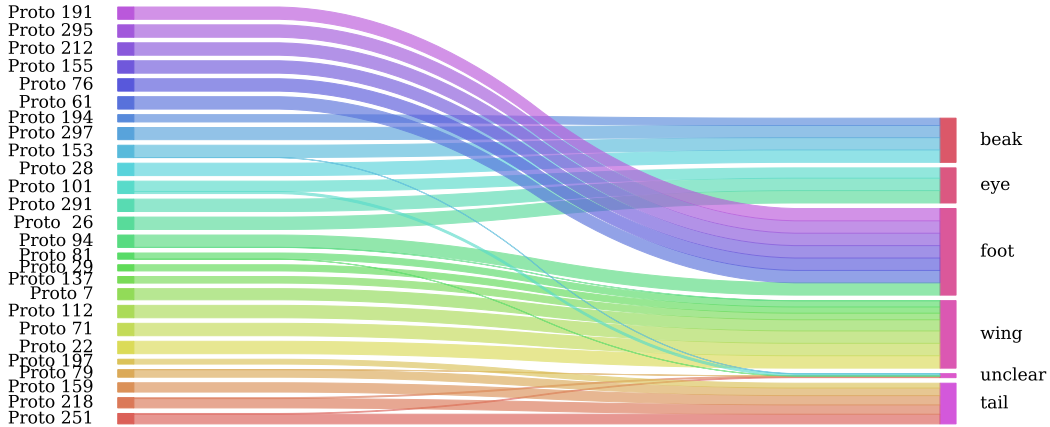


Figure 8: User-Study performed on the Funny-Birds datasets. The user was asked to assess the prototype visual consistency of the prototype (whether a prototype is associated to a specific bird part). 100 samples were visualised per prototype, when available (some prototypes were not present 100 times in the test set.)

The authors of the FunnyBirds dataset manually designed 5 bird parts: eyes (3 types), beak (4 types), wings (6 types), legs (4 types) and tail (9 types) to construct the 50 classes. As depicted in Figure 8, the learned prototypes were attributed consistently to the same parts with the following number of prototype per part: eye (3 prototypes), beak (4 prototypes), wings (7 prototypes), legs (7 prototypes) and tail (5 prototypes). These results are summarised in Figure 8. The consistency of the prototype was then evaluated by counting how many time each prototype highlighted the same region of the bird. It was found that 21 prototypes scored 100%, 2 prototypes scored 99%, 1 scored 93%, 1 scored 90%, and one scored 83%. For the eyes and beaks parts, the number of learned prototypes match exactly the number of bird part types. Each prototype can therefore be directly attributed to a specific part, e.g. prototype #101 relates to "eye0", prototype #297 relates to "beak1".. This user study allows to confirm the *meaningfulness* of the prototypes derived from the proposed architecture, as well as *compactness* of the explanations allowing direct comparison with how a human would approach the classification task. Full results for this study are found in the uploaded material can be found in Supplementary Materials [51].

H Consistency and stability metrics adaptation

The consistency and stability metrics initially developed by Huang et al. [53] were adapted to the FunnyBirds dataset. The aim was to allow a finer evaluation of the prototypes by taking advantage of the part-segmentation provided with this dataset. Both metrics are based for each image on the vector o_p . This vector is a binary vector indicating whether prototype p_j is related to category $q \in Q$. There are five categories for the FunnyBirds dataset: beak, eye, foot, tail and wing. For each category we set the entry of the vector o_p to one if an entry of the similarity map \mathcal{M}_j weighted by the importance of the corresponding prototype $i_{j,k}$ is larger than 0.1 within the binary segmentation mask corresponding to the given category N_q :

$$o_{p_j}^q = \max \{i_{j,k} (\mathcal{M}_j \circ N_c)\} > 0.1 \quad (7)$$

The consistency and stability scores are then evaluated using the same way formula as [53] with our modified vector o_p . However as the initial paper considers prototypical models where prototypes only belongs to one class, we repeat the operations across all classes. Only the prototype that appears in the prediction for the considered class are included and the result is averaged across all classes.